Silicon carbide membranes for micro-electro-mechanical-systems based CMUT with influence factors

Moumita Pal[1,2], Niladri Pratap Maity[1✉], Reshmi Maity[1]

[1]Department of Electronics and Communication Engineering, Mizoram University (A Central University),

Aizawl-796004, India

[2]Department of Electronics and Communication Engineering, JIS College of Engineering, Kolkata, India

✉ maity_niladri@rediffmail.com

Abstract. An analytical model is developed for evaluating the characteristic parameters of silicon carbide (SiC) based capacitive micromachined ultrasonic transducer (CMUT) under the effect of a high-k dielectric insulation layer. The performance of parallel plate structured CMUT is investigated by considering various widths of the insulation layer, membrane thickness, diameter, and bias followed by validation of results using finite element method (FEM) simulation. Consideration of the fringing effect results in noticeable improvements in device capacitance. This enhancement leads to improvement in displacement due to static bias, signal, and coupling coefficient. The comparative analysis is carried out between hafnium oxide (HfO_2) and silicon nitride (Si_3N_4) insulation layers. CMUT having HfO_2 insulation of 500 nm thickness exhibits resonance at 1.62 MHz and displacement of 405 nm. Approximately 20% enhancement occurs in displacement as compared with Si_3N_4 as insulation.
Keywords: CMUT, HfO_2 insulation, High-k dielectric material, SiC actuation layer

1. Introduction
Ultrasonic transducers are involved in medical imaging, which involves the usage of ceramics, different crystals of polymer, piezoelectric, and piezo composite materials. To overcome the shortcomings of piezoelectric transducers, micromachined ultrasonic transducers (MUTs) are introduced. Based on the variation of device capacitance CMUT works and thus modulation of electrostatic force takes place. This capacitive device is mostly involved in the emission and detection of ultrasonic waves [1-4]. The MEMS fabrication technique allows for the creation of CMUTs with high flexibility, low-temperature fabrication, downsizing, and, most importantly, good reproducibility. Significant advancements in material science have made it possible to use a wide choice of MEMS materials for fabrication, based on the prime needs in the various application domains. Metals like Ni (nickel), Al (aluminium), non-metals like Si (silicon), Ge (germanium), polymers like SU8, polyimide like diamond, SiC (silicon carbide), Si_3N_4 (silicon nitride), and SiO_2 (silicon dioxide) are utilised in membrane fabrication [5-8]. Many research have shown that the

structure and composition of the membrane have a significant impact on resonance frequency. Employing surface micromachining technology Si_3N_4 is used for fabricating both the membrane and the insulating layer material. Si is used as the membrane in another Si_3N_4-based CMUT, and SiO_2 is used to form insulation layer in transducers fabricated by wafer-bonding technique. [9-11].

Modeling a CMUT cell with a circular Si_3N_4 membrane and varied electrode configurations is used to investigate the effects of collapse and snapback voltage. The CMUT's static finite element calculations were validated using a licenced FEM application (PZFlex) [12-13]. Applying bias to the structure, an equivalent swing will take place due to the membrane's displacement while operating in transmission mode. Electrostatic force holds a non-linear relationship for the bias to the transduction gap [14], hence, to operate at a low voltage effectively, transduction gap between top and bottom electrodes is to be reduced. Considering all the limitations caused by fabrication, transmission of desired pressure at operating frequency is only possible by maintaining a minimum transduction gap. During a complete swing in transmission mode and a collapsed condition in receiving mode, the distance between the top and bottom electrodes can be spanned, which results in an electrical shock. As a precaution against being affected by electric shock, a dielectric layer must now be presented. Due to electrostatic attraction force, the insulating layer must withstand the generated electric field in the device.

In addition to this during collapsed mode also electrodes get separated due to this insulation layer [14-15]. Inclusion of the insulation layer reduces both the electric field and device capacitance as separation between two electrodes increases, so to retain the same membrane displacement the choice of a dielectric layer is an essential factor for determining the performance. The parameters can be rescued from having detrimental value by laying the actuation layer patterning above the top electrode. In case of less separation gap, the generated electrostatic pressure is a much smaller value compared to Van der Waals pressure. When the top electrode approached the bottom electrode and made contact, it remained stuck due to the low energy level, as the total removal energy reached a minimum level. This total energy is made up of energy that has been restored due to the surface's deformation and attraction.

Analytical modeling [16] is well demonstrated about a SiC-based CMUT having an insulation layer of Si_3N_4 having a 110 µm diameter membrane. A resonance of 1.65 MHz is exhibited by this CMUT array which consists of higher device capacitance, enhanced displacement in the membrane, larger coupling factor, and lower collapse voltage as compared to a non-insulated counterpart with the same device dimension. As a transducer, the features of the insulated construction are desirable. All of the results are compared to FEM, and there is a lot of consistency. The use of a high-k dielectric material improves the effectiveness of creating a high electric field while keeping the transduction gap the same. Moreover further increase of bias is not required for both in transmitting and receiving mode.

In this paper, a comparative analysis is done based on different high- k dielectric materials [17-19] strongly supported by FEM simulation outcomes.

2. Structure of insulated CMUT with silicon carbide-based membrane

CMUT is a capacitive device having metalized membrane upon a top electrode and another bottom electrode [20-27]. The insulating layer is developed by patterning the top electrode just below the thin metalized membrane of 2 µm and electrode diameter of 110 µm forming one of the electrodes over a tiny gap of 450 nm over the entirely doped Si in an insulated element as shown in Fig. 1.
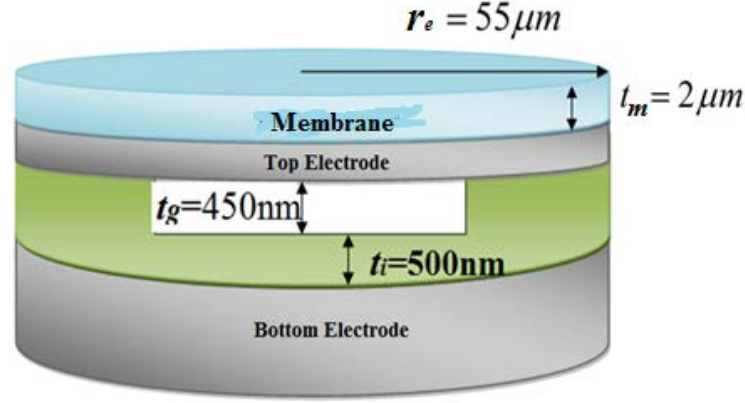
$$r_e = 55 \mu m$$

Fig. 1. 3D model of insulated CMUT

3. Proposed analytical model

Considering the fringing effect by Landau and Lifschitz's approach [16], the gap capacitance is C_{gf} and C_{if} is the same for the insulation layer. This gives, the following equations respectively

$$C_{gf} = \varepsilon_g \left[\left(\frac{\pi r_e^2}{t_g} \right) + r_e \ln \left\{ \left(\frac{16 \pi r_e}{t_g} \right) - 1 \right\} \right], \tag{1}$$

$$C_{if} = \varepsilon_a \left[\left(\frac{\pi r_e^2}{t_i} \right) + r_e \ln \left\{ \left(\frac{16 \pi r_e}{t_i} \right) - 1 \right\} \right]. \tag{2}$$

Now C_{eqf} is considered as the equivalent series capacitance due to fringing for both the insulation layer and the air gap. As a result, an insulated structure's equivalent device capacitance can be represented as

$$C_{eqf} = \frac{\left\{ \frac{\pi r_e}{t_g} + \ln\left(\frac{16\pi r_e}{t_g} - 1\right) \right\} \left\{ \frac{K_i \pi r_e}{t_i} + K_i \ln\left(\frac{16\pi r_e}{t_i} - 1\right) \right\}}{\left\{ \frac{\pi r_e}{t_g} + \ln\left(\frac{16\pi r_e}{t_g} - 1\right) \right\} + \left\{ \frac{K_i \pi r_e}{t_i} + K_i \ln\left(\frac{16\pi r_e}{t_i} - 1\right) \right\}}. \tag{3}$$

Here, t_g is denoted for the air gap, t_i is the width of the insulation layer and the area of the electrodes is represented by $A = \pi r_e^2$, where r_e is the electrode radius. Permittivity of the insulating layer is expressed as $K_i \varepsilon_g = \varepsilon_i$, the dielectric constant of the insulation layer is K_i, the gap permittivity value ε_g is 8.85×10^{-12} C^2/(N-m^2). Generally, the electrostatic force due to fringing can be expressed as

$$F_f = \frac{1}{2} \left\{ \frac{v(t)^2 C_{if}^2}{C_{gf}^2 \left(\frac{C_{if}}{C_{gf}} + 1 \right)^2} \right\} \left[\varepsilon_g \left(\frac{\pi r_e^2}{t_g^2} \right) + \frac{\varepsilon_g r_e}{\left(\frac{16 \pi r_e}{t_g} - 1 \right)} \times \left(\frac{16 \pi r_e}{t_g^2} \right) \right]. \tag{4}$$

A large bias is rendered along the signal to produce an observable amount of electrostatic force at resonance. Mason's analysis can be used to determine the mechanical

behaviour of the CMUT membrane. The motion of a membrane under strain will be expressed as

$$\left\{ \frac{(Y_m + T_m)t_m^3}{12(1-\sigma_m^2)} \right\} \nabla^4 w_m - (T_m)\nabla^2 w_m - P + t_m \rho_m \left(\frac{\partial^2 w_m}{\partial t^2} \right) = 0. \tag{5}$$

Here t_m is the membrane thickness, Y_m is Young's modulus of the membrane, σ_m is the Poisson ratio and w_m is the membrane displacement involving Mason's model, T_m is the membrane tension and ρ_m is the material density of actuating material. For an insulated element with a fringing effect, the peak displacement at the centre under static bias becomes

$$w_{m_{bias}} = \left(\frac{1}{8AT_m} \right) \left\{ \frac{V_{dc}^2 C_{if}^2 r_m^2}{\left(\frac{C_{if}}{C_{gf}} + 1 \right)^2 C_{gf}^2} \right\} \times \left[\left(\frac{\varepsilon_g \pi r_e^2}{t_g^2} \right) + \left(\frac{\varepsilon_g r_e}{\left(\frac{16\pi r_e}{t_g} \right) - 1} \right) \times \left(\frac{16\pi r_e}{t_g^2} \right) \right]. \tag{6}$$

The dynamic response is carried out due to the application of signal in the device and is given by

$$w_{signal}(r) = \frac{P_{signal}}{\omega^2 \rho_m t_m} \left\{ \left(J_0\left(\frac{\omega}{\upsilon} r\right) \middle/ J_0\left(\frac{\omega}{\upsilon} r_m\right) \right) - 1 \right\}. \tag{7}$$

The description of the membrane's Z_m acoustic impedance is now essential for the model's correct calculation. The measurement of effective mechanical impedance of the membrane is carried out by the ratio of the applied pressure to the surface's average velocity. Estimation of the volume velocity through the device is attained by integrating the velocity given by $w_m(r_m,t)$ over the surface, considering the entire circular membrane.

$$V_{total} = \int_0^{r_m} \left(\dot{w}(r_m,t) \right)(2\pi r_m)dr_m = 2\pi \int_0^{r_m} \left(\dot{w}(r_m,t) \right) r_m dr_m = j2\pi\omega \int_0^{r_m} w(r_m)r_m dr_m. \tag{8}$$

The applied pressure to the surface's average velocity will be given by

$$V_{average} = \frac{j2\pi\omega}{\pi r_m^2} \int_0^{r_m} w(r_m)r_m dr_m = \frac{j2}{r_m^2} \frac{P_{signal}}{\omega\rho_a t_a} \left[\frac{1}{J_0(kr_m)} \int_0^{r_m} r_m J_0(kr_m)dr_m - \int_0^{r_m} r_m dr_m \right]. \tag{9}$$

Employing the well-known integral, $\int r J_0(kr)dr = \frac{J_1(kr)}{k}$, The membrane's effective mechanical impedance is defined as

$$Z_m = \left[\frac{-j\omega\rho_a t_m kr_m J_0(kr_m)}{2J_1(kr_m) - kr_m J_0(kr_m)} \right]. \tag{10}$$

For a capacitive element, measurement of collapse voltage is quite an impacted factor while operated at its best working point. The operating bias applied to the MUT determines its performance. Different operating modes exist based on the membrane's behaviour under static conditions, such as collapsed mode and conventional mode. The electrostatic force generated by the applied DC voltage pulls the membrane towards the substrate, which is countered by the membrane's mechanical restoring force. An increase in bias also enhances membrane displacement. A voltage imbalance between these restorative and electrostatic forces occurs over a specific voltage, causing the membrane to collapse down onto the substrate. The mathematical analysis is initiated with the assumption that the sum of the capacitor and spring forces actuates mass, hence the equation is expressed as

$$F_{CAPACITOR} + F_{SPRING} = F_{MASS}. \tag{11}$$

Hence, the collapse voltage can be expressed as

$$V_{collapse} = \sqrt{\frac{8K_m\left(t_g + \left(\frac{\varepsilon_g}{\varepsilon_i}\right)t_i\right)^3}{27\varepsilon_g A}} , \qquad (12)$$

where K_m is the spring constant. The dimensionless factor coupling coefficient is a characterization parameter that measures the energy transformation capability of the transducer from one type to another. Most influencing parameters that have a great impact on coupling coefficients are stress distribution, presence of the electric field, and cell geometry, as well as the type of material, all of which influence coupling coefficients [16]. The dynamic coupling factor is expressed as

$$k_w = \sqrt{\frac{\varepsilon_g A V_{dc}^2}{\varepsilon_g A V_{dc}^2 + 26.28 \times (P_r t_m d_{eff}^3)}} , \qquad (13)$$

where,

$$d_{eff} = \left(t_g + \frac{\varepsilon_g}{\varepsilon_i}t_i\right) . \qquad (14)$$

4. Results and Discussion

A mathematical model is used to investigate the capacitance behaviour, collapse voltage, and coupling factor of the CMUT. For optimizing the device's energy conversion, sensitivity, operating point, and efficiency, all the factors should be considered. A smaller gap and thinner insulator suggest a closer distance between the pair of electrodes, resulting in a higher voltage across the plates (field force) and charge composed on the plates (flux) for any voltage applied across the two electrodes, resulting in larger capacitance. Materials with a high dielectric constant have a higher permittivity than materials with a lower permittivity, allowing them to suggest less field flux disagreement for a given field force. All of these results may be deduced from a simple observation of ordinary capacitor plates, and the analytical model can be used to calculate capacitance for any pair of unconnected conductors. FEM simulation is used to verify all of the results. At a 55 µm membrane radius, the device capacitance calculated for the CMUT is 0.163 pF, providing a force of 1.263 µN.
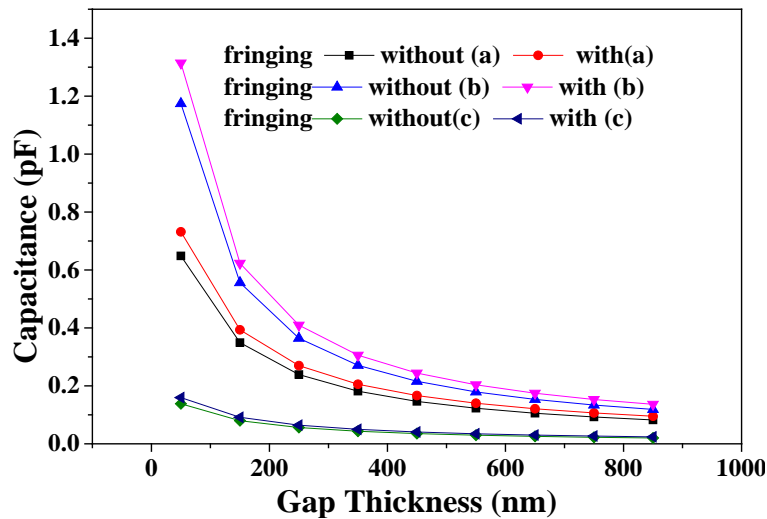

Fig. 2. Capacitance of the device with varying width of air gap for a) $r_e = 55$ µm, $t_i = 500$ nm, b) $r_e = 65$ µm, $t_i = 300$ nm, c) $r_e = 27.5$ µm, $t_i = 650$ nm

Figure 2 depicts the variance in device capacitance as a function of gap thickness. With regard to gap thickness, the capacitance drops in a parabolic way. The device capacitance is higher when the electrode radius is larger and the insulation thickness is thinner. As seen in Fig. 3, the gap thickness increases the fringe capacitance.

The fringing effect is amplified by greater gap thickness, smaller electrode radius, and larger valued insulation thickness. An average E'_C of 13.27% enrichment takes place for $t_g = 650$ nm, $t_i = 300$ nm, and 16.79% for $t_g = 300$ nm, $t_i = 650$ nm.
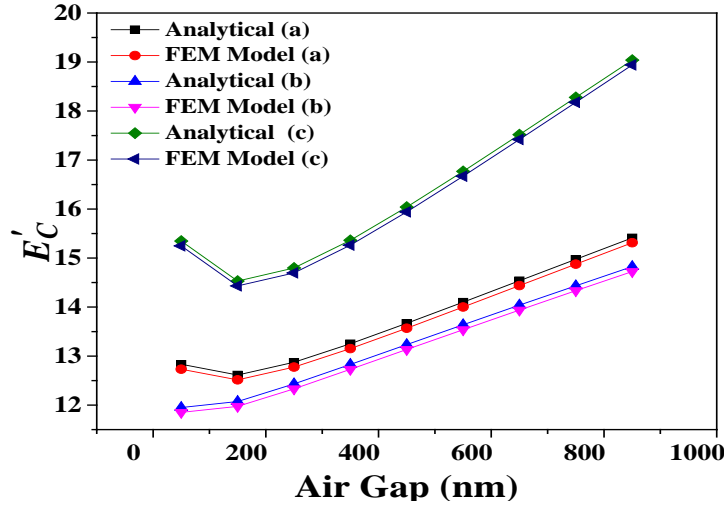

Fig. 3. E'_C with respect to air gap for a) $r_e = 55$ µm, $t_i = 500$ nm, b) $r_e = 65$ µm, $t_i = 300$ nm, c) $r_e = 27.5$ µm, $t_i = 650$ nm

Figure 4 illustrates the electrostatic force as a function of insulation thickness, with the electrostatic force decreasing as the insulation thickness of the dielectric layer increases. It is critical to select the proper dielectric insulation thickness because it is one of the determining factors in producing excellent accuracy and electrostatic force. Figure 5 further indicates that the fringing approach improves electrostatic force significantly with respect to insulation thickness. The fringing effect has a bigger impact above 300 nm of insulation thickness and lesser in lower values. An average value E'_F of 11.24% is observed by changing the insulation thickness while designing is done.
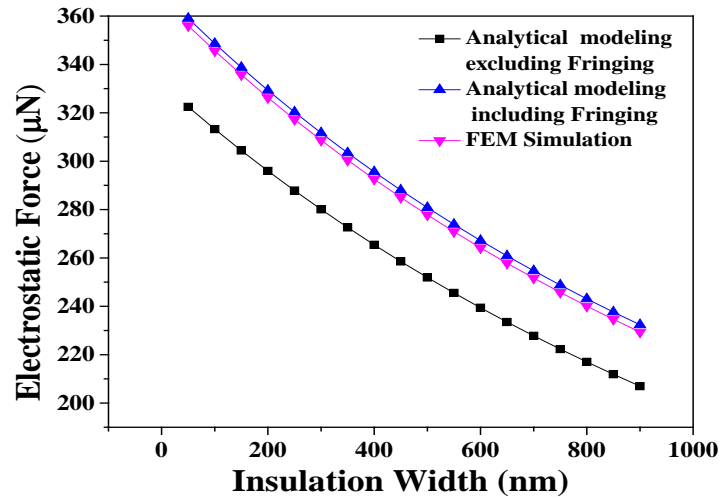

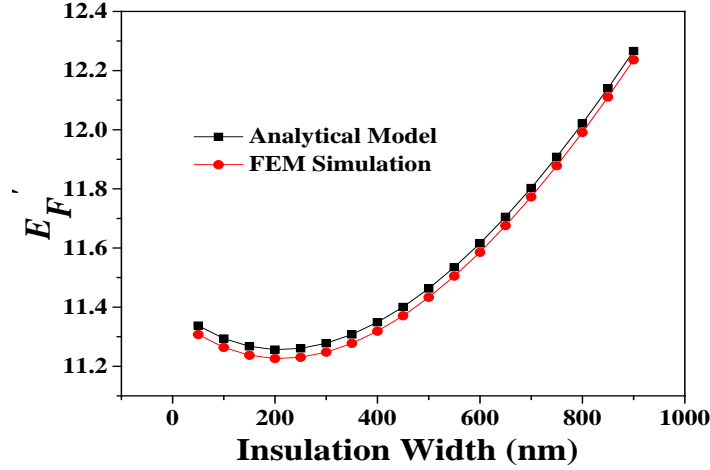**Fig. 4.** For variable insulation layer thicknesses, electrostatic force is used

Fig. 5. $E_F^{'}$ for varying thickness of insulation layer

Figure 6 illustrates that when the membrane radius is at its largest, the material permittivity displacement is at its highest. The figure depicts the changing type of membrane displacement as both parameters are increased. Displacement decreases as insulation thickness increases, resulting in maximum displacement at the minimum insulation width and maximum membrane radius, as shown in Figure 7.

The coupling capacitance reduces as the coupling distance (effective gap distance) grows, diminishing the intensity of the output energy. The membrane in CMUT transports in the presence of an applied electric field, with no transverse membrane vibration. In a CMUT, the coupling distance is also influenced by the gap distance and insulator thickness. At a bias voltage of 40 V DC, the coupling factor of the proposed structure is 0.384, indicating that the CMUT's coupling efficiency is 38.3 percent. When the surface tension of the membrane increases, the surface area of the membrane reduces, diminishing the coupling capacitance and the coupling factor. CMUTs have been shown in numerous investigations to work in both the conventional and collapse modes. The predicted collapse voltage is 78.16 V, with a coupling factor of 0.7, indicating that increasing the coupling factor has a substantial impact on transducer efficiency. The collapse voltage characteristics indicate that the collapse voltage decreases with increasing membrane radius and increases with increasing membrane thickness. This is connected with the fact that when the membrane's spring constant decreases, it becomes less stiff, and when it increases, it becomes stiffer, resulting in greater elasticity. FEM simulation is also used to validate all of the data.
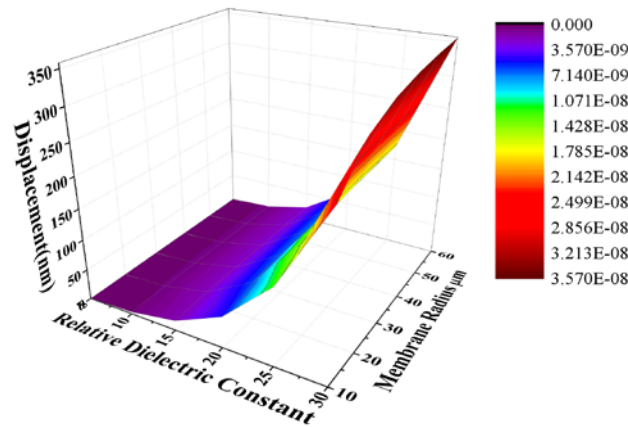

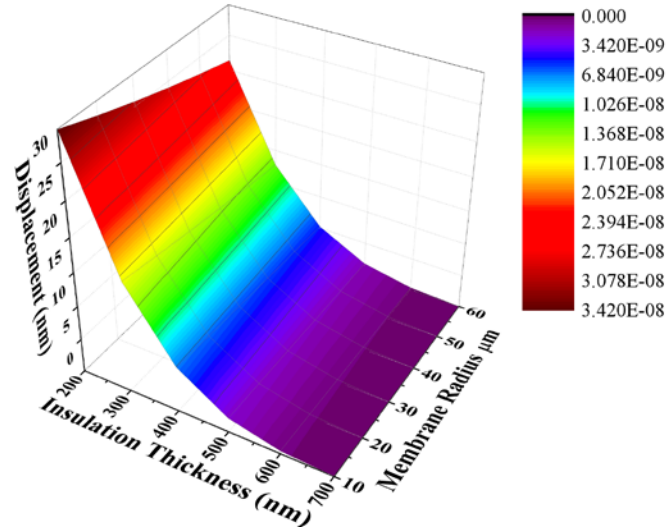**Fig. 6.** Deviation of static displacement with simultaneous change in r_m and K

Fig. 7. Deviation of static displacement with simultaneous variation in r_m and t_i

Figure 8 depicts the variation of the membrane's spring constant and collapse voltage with changing membrane radius. Because the collapse voltage has a linear connection with the spring constant, an increase in radius reduces the spring constant. Furthermore, as demonstrated in Fig. 9, a decrease in membrane thickness lowers the collapse voltage value.
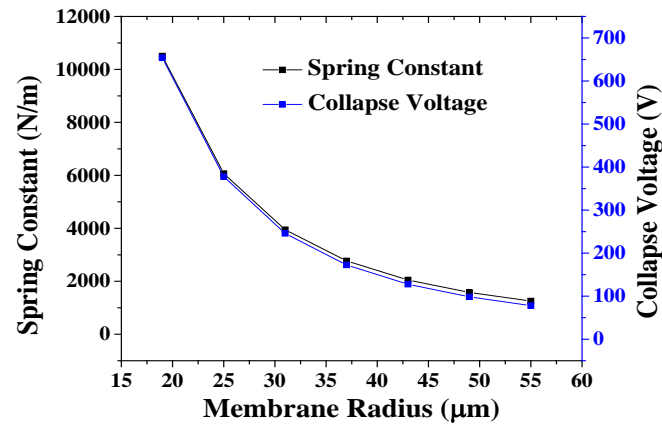

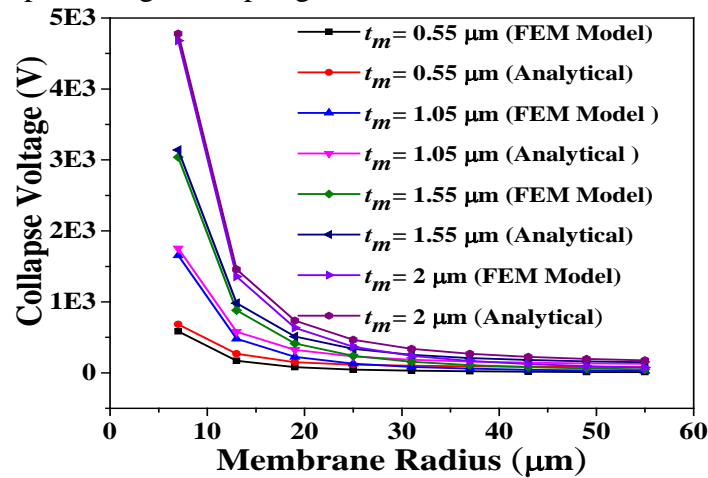**Fig. 8.** Collapse voltage and spring constant as functions of a membrane radius

Fig. 9. Changes in collapse voltage when the membrane radius changes due to varied membrane thickness values

Figure 10 represents the variation of 3D displacement as a feature of frequency and membrane radius. The displacement of the membrane has maximum at the device's centre point. The resemblance of the designed structure's resonance during AC actuation, where resonance can be seen at 1.62 MHz [18], can be used for further validation. The resonance displacement is a maximum of 50 Å which matches the displacement shown in the constructed structure and is validated by simulation results. The presence of several resonances in CMUT is observed, as shown in the image. At first resonance, the maximum amplitude is observed, with sole dependency upon material usage and geometrical features of the device. The mechanical impedance is determined by the pressure-to-velocity ratio at the membrane's centre. As shown in Fig. 11, by obtaining the displacement with a particular pressure load, the variation of mechanical impedance can be measured. At the device resonance frequency, overall impedance is reduced to a minimum.
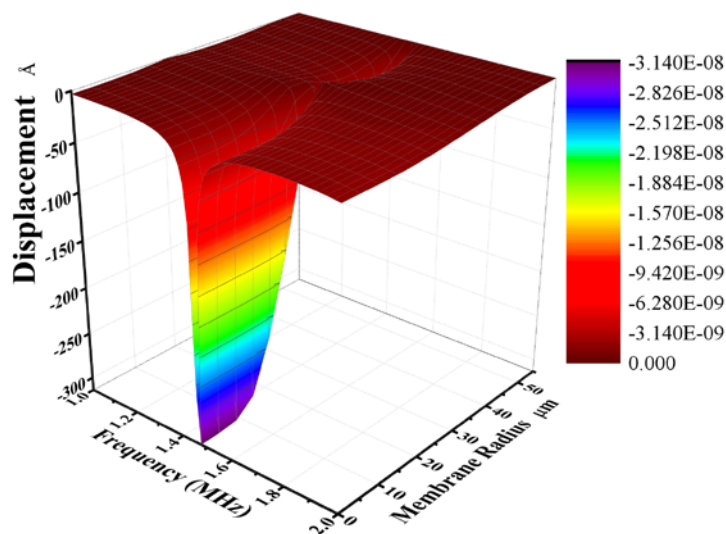

Fig. 10. 3D Frequency response of 110 μm actuated membrane
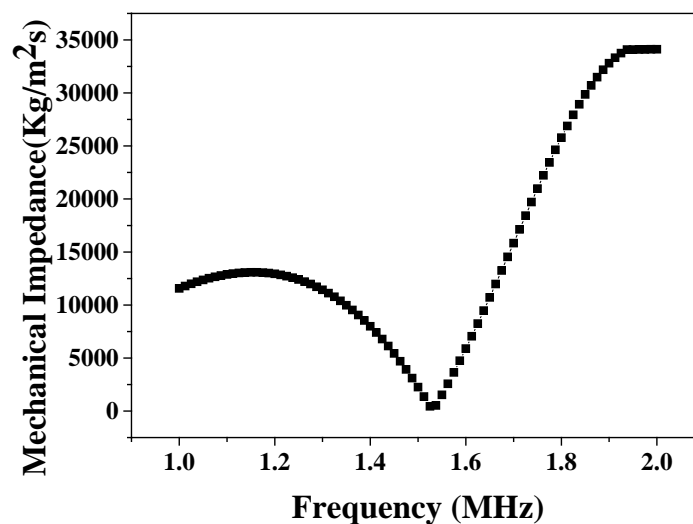

Fig. 11. Impedance profile as a function of frequency

5. Conclusion

The general functionality of SiC membranes CMUT is demonstrated in this study, along with its influencing factors. Higher sensitivity is achieved when the device capacitance is greater than the force exerted by the membrane. To achieve a high-sensitivity CMUT, the

transduction gap and insulator layer thickness must be extremely thin, with a wide membrane radius, and the insulating layer material must have a high relative permittivity. A novel approach to fringing field capacitance is also included in the characteristic study of SiC-based CMUT. When compared to PECVD Si_3N_4, the performance of CMUT is superior in all respects. This increase in CMUT parameters will surely improve its sensitivity for high-frequency applications and in the acoustic medium. The AC response and impedance profile of the CMUT element were simulated using Mason's model for circular-shaped devices. Theoretical findings are supported by simulation findings, leading to even greater agreement. The imitative analytical model for the vented capacitive element contains multiple resonances. Because main resonance has a greater peak value displacement than secondary resonance, it will take precedence over secondary resonance. Because of its matched impedance to air and water, the device is suitable for both acoustic and air mediums. In this case, the coupling coefficient is around 0.67, and it is higher for thinner but larger-diameter membranes. In terms of membrane material, SiC outperforms Si_3N_4 as a structural layer in larger deformation and high-frequency implementations.

References
1. Hasan A, Nurunnabi M, Morshed M, Paul A, Polini A, Kuila T, Hariri M, Lee Y, Jaffa A. Recent advances in application of biosensors in tissue engineering. *BioMed Research International.* 2014;2014: 1-18.
2. Ramadoss R, Dean R, Xiong X. MEMS testing. In: *System-on-Chip Test Architectures.* 2008. p.591-651.
3. Mills DM. Medical imaging with capacitive micromachined ultrasound transducer (cMUT) arrays. *IEEE Ultrasonics Symposium Proceedings.* 2004;1: 384-390.
4. Ladabaum I, Jin X, Soh HT, Atalar A. Khuri-Yakub BT. Surface micromachined capacitive ultrasonic transducers. *IEEE Transactions on Ultrasonics, Ferroelectrics, and Frequency Control.* 1998;45(3): 678-690.
5. Logan A, Yeow JT. Fabricating capacitive micromachined ultrasonic transducers with a novel silicon-nitride-Based wafer bonding process. *IEEE Transaction on Ultrasonics, Ferroelectrics and Frequency Control.* 2009;56(5): 1074-1084.
6. Cetin M, Bayram, B. Diamond-Based Capacitive Micromachined Ultrasonic Transducers in Immersion. *IEEE Transaction on Ultrasonics, Ferroelectrics and Frequency Control.* 2013;60(2): 414-420.
7. Gerardo D, Cretu E, Rohling R. Fabrication and testing of polymer-based capacitive micromachined ultrasound transducers for medical imaging. *Microsystems & Nanoengineering.* 2018;4(19): 568-579.
8. Maity R, Maity NP, Rao KS, Guha K, Baishya S. A new compact analytical model of nanoelectromechanical systems-based capacitive micromachined ultrasonic transducers for pulse echo imaging. *Journal of Computational Electronics.* 2018;17(3): 1334-1342.
9. Huang Y, Zhuang X, Haeggstrom EO, Ergun AS, Cheng CH, Khuri-Yakub BT. Capacitive micromachined ultrasonic transducers with piston-shaped membranes: Fabrication and experimental characterization. *IEEE Transactions on Ultrasonics, Ferroelectrics, and Frequency Control.* 2009;56(1): 136-145.
10. Caronti A, Caliano G, Iula A, Pappalardo M. An accurate model for capacitive micro machined ultrasonic transducers. *IEEE Transactions on Ultrasonics, Ferroelectrics, and Frequency Control.* 2002;49(2): 159-168.
11. Lohfink A, Eccardt P. Linear and nonlinear equivalent circuit modeling of CMUTs. *IEEE Transactions of Ultrasonics, Ferroelectrics, and Frequency Control.* 2005;52(12): 2163-2172.

12. Nikoozadeh A, Bayram B, Yaralioglu G, Khuri-Yakub BT. Analytical calculation of collapse voltage of CMUT membrane. *IEEE Ultrasonics Symposium Proceedings*. 2004;1: 256-259.

13. Koymen H, Atalar A, Aydogdu E, Kocabas C, Oguz HK, Olcum S, Ozgurluk A, Unlugedik A. An improved lumped element nonlinear circuit model for a circular CMUT cell. *IEEE Transactions on Ultrasonics, Ferroelectrics, and Frequency Control*. 2012;59(8): 1791-1799.

14. Wygant IO, Kupnik M, Khuri-Yakub BT. Analytically calculating membrane displacement and the equivalent circuit model of a circular CMUT cell. *IEEE Ultrasonics Symposium*, 2008: 2111-2114.

15. Maity R, Maity NP, Thapa RK, Baishya S. Investigation of Si_3N_4 as an Excellent Membrane Material for MEMS Ultrasonic Transducers. *Applied Mechanics and Materials*. 2017;45: 567-571.

16. Pal M, Lalengkima C, Maity R, Baishya S, Maity NP. Effects of fringing capacitances and electrode's finiteness in improved SiC membrane based micromachined ultrasonic transducers. *Microsystem Technologies*. 2021;27: 3679-3691.

17. Panchanan S, Maity R, Baishya S, Maity NP. Modeling, simulation and analysis of surface potential and threshold voltage: application to high-K material HfO_2 based FinFET. *Silicon*. 2021;13(1): 3271-3289.

18. Maity NP, Maity R, Maity S, Baishya S. A new surface potential and drain current model of dual material gate short channel metal oxide semiconductor field effect transistor in sub-threshold regime: application to high-k material HfO_2. *Journal of Nanoelectronics and Optoelectronics*. 2019;14(6): 868-876.

19. Chakrabarti H, Maity R, Baishya S, Maity NP. An accurate model of threshold voltage and effect of high-k material for fully depleted graded channel DMDG MOSFET. *Silicon*. 2022. DOI: 10.1007/s12633-021-01412-w.

20. Maity R, Suvra S, Maity S, Maity NP. Collapse voltage analysis of central annular ring metallized membrane based MEMS micromachined ultrasonic transducer. *Microsystem Technologies*. 2020;26: 1001-1009.

21. Pal M, Maity NP, Maity R. An improved displacement model for micro-electro-mechanical-system based ultrasonic transducer. *Microsystem Technologies*. 2019;25: 4685-4692.

22. Maity R, Gogoi K, Maity NP. Micro-electro-mechanical-system based capacitive ultrasonic transducer as an efficient immersion sensor. *Microsystem Technologies*. 2019;25: 4663-4670.

23. Maity R, Maity NP, Baishya S. An efficient model of nanoelectromechanical systems based ultrasonic sensor with fringing field effects. *IEEE Sensors Journal*. 2020;20(4): 1746-1753.

24. Maity R, Maity NP, Guha K, Baishya S. Analysis of fringing capacitance effect on the performance of micro-electromechanical-system-based micromachined ultrasonic air transducer. *IET Micro and Nano Letters*. 2018;13(6): 872-876.

25. Maity R, Maity NP, Thapa RK, Baishya S. Analysis of frequency response behaviour of capacitive micromachined ultrasonic transducers. *Journal of Computational and Theoretical Nanoscience*. 2015;12(10): 3492-3494.

26. Maity R, Maity NP, Thapa RK, Baishya S. Analytical characterization and simulation of a 2-D capacitive micromachined ultrasonic transducer array element. *Journal of Computational and Theoretical Nanoscience*. 2015;12(10): 3692-3696.

27. Maity R, Singh A, Islam A, Maity NP, Thapa RK, Baishya S. Lumped electromechanical modeling of capacitive micromachined ultrasonic transducers. *Journal Materials Today: Proceedings*. 2016;3(6): 2289-2294.

THE AUTHORS

Moumita Pal
e-mail: moumitajisceece@gmail.com
ORCID: 0000-0002-8665-478X

Niladri Pratap Maity
e-mail: maity_niladri@rediffmail.com
ORCID: 0000-0002-1256-5856

Reshmi Maity
e-mail: reshmidas_2009@rediffmail.com
ORCID: 0000-0002-1254-3075